TOWARDS THE RECONCILIATION OF VISCOSITY CHANGE AND CO_2-INDUCED POLYMERIZATION IN SILICATE MELTS

Yann MORIZET[1], Michael PARIS[2], David SIFRE[3], Ida DI CARLO[3], Sandra ORY[4], Fabrice GAILLARD[3]

[1] Université de Nantes, Nantes Atlantique Universités, Laboratoire de Planétologie et Géodynamique de Nantes (LPG), UMR CNRS 6112, 2 rue de la Houssinière, 44322 NANTES (France)

[2] Institut des Matériaux Jean Rouxel (IMN), Université de Nantes, UMR CNRS 6502, 2 rue de la Houssinière, BP32229, 44322 NANTES Cedex 3 (France)

[3] CNRS/INSU-Université d'Orléans – BRGM, UMR 7327, Institut des Sciences de la Terre d'Orléans, 1A rue de la Férollerie, 45071, Orléans, France

[4] CNRS-CEMHTI Conditions Extrêmes et Matériaux: Haute Température et Irradiation, UPR 3079, 1D avenue de la Recherche Scientifique, 45071, Orléans, France

Corresponding author: Yann Morizet

Postal address:

Laboratoire de Planétologie et Géodynamique de Nantes (LPG Nantes), UMR-CNRS 6112, Université de Nantes.

2 rue de la Houssinière, 44322 Nantes Cedex (FRANCE)

phone: +33 (0) 2 5112 5491

fax: +33 (0) 2 5112 5268

*E-mail: yann.morizet@univ-nantes.fr

Abstract:

Deep mantle melts contain massive amounts of CO_2 but three critical issues related to the effect of CO_2 on molecular structure and physical properties of magmatic melts remain poorly constrained: 1) there is no exact picture of CO_2 dissolution mechanism in silicate melt, 2) the silicate melt polymerization upon CO_2 dissolution has not been reliably quantified and 3) the effect of CO_2 on silicate melt viscosity has never been measured adequately.

We synthesized a series of ^{17}O and ^{29}Si-enriched CO_2-bearing melilitite (SiO_2 ~ 35 wt.%) silicate glasses at high temperature and pressure. Using NMR spectroscopy, we have interrogated both anionic and cationic networks for quantifying the change in the degree of polymerization associated to CO_2 incorporation in the melt. Increasing CO_2 content induces a strong increase in the degree of polymerization. CO_2 dissolution follows a complex mechanism involving the formation of Free Ionic Carbonate (FIC) $Ca^{2+}..CO_3^{2-}$ species. This carbonate subnetwork is the precursor to the immiscibility process between a carbonate liquid and a silicate liquid.

Glass transition temperature (Tg) measurements show that increasing CO_2 content induces a decrease in Tg implying a decrease in viscosity for the studied low silica melt composition. This result appears in complete contradiction with the melt polymerization induced by CO_2 as quantified by NMR. We propose a model that reconciles both aspects. CO_2 induces silicate subnetwork polymerization resulting in a viscosity increase but it also induces a competing effect by forming a carbonate subnetwork having a low viscosity. The overall result appears dominated by the carbonate subnetwork resulting in a slight decrease in melt viscosity in agreement with existing studies.

Number of word: 265

Keywords: CO_2 dissolution mechanism, low silica melt polymerization, CO_2 effect on silicate melt viscosity.

1. Introduction:

Carbon dioxide (CO_2) is a ubiquitous component of the Earth's mantle and it is known to play a major role in the mantle melting (Wyllie and Huang, 1976; Taylor and Green, 1988; Wallace and Green, 1988; Dasgupta and Hirschmann, 2006; Dasgupta, 2013). Melts with low silica content (< 40 wt.%) and high CO_2 content are broadly produced by low degree partial melting (Massuyeau et al., 2015) over a great depth interval and are possibly affecting large scale geophysical observations such as electrical conductivity as shown by Sifré et al. (2014). A key question related to their physical properties (i.e. viscosity) is: how fast such buoyant melts move through the surrounding mantle? Silicate melts and carbonate melts at mantle conditions have been well studied while the intermediate CO_2-rich silicate (e.g. melilitites and nephelinites), which are prevailing in the mantle (Mitchell, 2005) have poorly defined physical properties. To circumvent the experimental difficulties in measuring viscosity in CO_2-bearing silicate melt, one method often quoted is to scrutinize the change in the silicate melt molecular structure upon CO_2 dissolution to gain access to the melt viscosity (Stebbins, 2016).

Pioneer works (Eggler, 1978; Mysen and Virgo, 1980a) on CO_2 dissolution in silicate melt conjectured that CO_2 acts as a polymerizing agent hence increasing melt viscosity. The suspected CO_2 dissolution involves the polymerization (i.e. increasing connectivity of the oxygen atoms) of the structural units (Mysen and Virgo, 1980b; Q^n species where Q is a tetrahedral unit with n bridging oxygens) with the following reaction:

$$CO_2^{fluid} + 2Q^{n\,melt} \leftrightarrow CO_3^{2-\,melt} + 2Q^{n+1\,melt} \qquad \text{Eq. 1}$$

Where a CO_2 molecule scavenges an available oxygen of a Q^n unit to form a free $M^{n+}..CO_3^{2-}$ group in which M^{n+} is a charge balancing or network modifying cation (e.g. Ca^{2+}). As Eq. 1 proceeds to the right, there is a change in the proportion of the different oxygen species: a

Non-Bridging Oxygen (NBO) is consumed by the CO_2 molecule and a Bridging Oxygen (BO) is produced. The proportion of both oxygen species defines the degree of polymerization. Although this mechanism appears intuitively acceptable, it has never been reliably determined experimentally. Recent work using ^{29}Si MAS NMR spectroscopy (Morizet et al., 2014b; Moussallam et al., 2016) attempted to quantitatively measure the change in polymerization upon CO_2 dissolution and corroborated the polymerizing effect of CO_2. However, simple mass balance calculations using Eq. 1 do not match the calculations made from ^{29}Si NMR spectra: the increase in polymerization is too large for the amount of CO_2 dissolved. This lack of internal consistency shows the difficulty of the ^{29}Si NMR method and suggests that a more complex structural mechanism is at stake for CO_2 dissolution in silicate melts . This mechanism could involve changes: 1) in the distribution of the structural units (Q^n species), and 2) in the distribution of bond length and angles within the structural units (Lee, 2004, 2005; Massiot et al., 2012).

As a result, a reliable quantification of the silicate degree of polymerization upon CO_2 dissolution with spectroscopic methods needs to be carefully conducted. One problem arises from the fact that the measurement of the degree of polymerization in the melt has been always approached from the cationic view side (^{29}Si MAS NMR mainly) which is easily accessible from the experimental point of view. However, the determination of the degree of polymerization is hindered by the strong influence of the silicate melt chemical composition on the ^{29}Si peak position and the strong overlapping in between individual spectral lines (Engelhardt et al., 1985; Schmidt et al., 2000; Hiet et al., 2009).

Although ^{17}O MAS NMR is less accessible and the available data on silicate glasses are rare, it is recognized as a powerful tool for determining the degree of polymerization in silicate glasses (Farnan et al., 1992; Stebbins et al., 2001; Alwardt and Stebbins, 2004; Lee and Stebbins, 2009) by probing the different oxygen species. The reason being that the spectral

distribution of the different kind of oxygens, Bridging (BO) and Non-Bridging Oxygen (NBO), in a silicate glasses is directly distinguished and consequently the degree of polymerization expressed as the NBO/T (number of NBO per Tetrahedron) is readily determined.

In the present work, we have investigated the change in the degree of polymerization as a function of CO_2 content in a silicate glass composition close to melilitite composition using ^{17}O and ^{29}Si NMR spectroscopy. Both results obtained by ^{17}O and ^{29}Si NMR spectroscopy are compared and point towards an increase in the degree of polymerization of the silicate network structure. We clarify the CO_2 dissolution mechanism in the studied silica undersaturated glass composition. Calorimetric measurements of the glass transition temperatures (Tg) suggest a decrease in viscosity with increasing CO_2 content. The inconsistency between spectroscopy and calorimetry is discussed and we propose reconciliation to both aspects. We conclude with a first order model for silicate melt viscosity as a function of CO_2 content.

2. Experimental method:

We synthesized at high pressure (between 0.5 and 1.5 GPa) a series of silicate glasses with composition analogous to melilitite melt (Brooker et al., 2001; Bosshardt-Stadlin et al., 2014) in the Na_2O-CaO-Al_2O_3-SiO_2 system: ~35 wt.% SiO_2 and NBO/T = 2 calculated from the stoichiometric chemical composition corresponding to a highly depolymerized composition (see Table 1). The composition was prepared from a mixture of oxides (Al_2O_3 and SiO_2) and carbonate (Na_2CO_3 and $CaCO_3$). For NMR acquisition, we used ^{17}O and ^{29}Si isotopically enriched oxides: $^{29}SiO_2$, $Si^{17}O_2$ and $Al_2{}^{17}O_3$; the resulting starting composition was enriched at ~10 and ~40 mol.% in ^{17}O and ^{29}Si, respectively.

The $CaCO_3$ and the Na_2CO_3 are the source of CO_2 during the experiments. Except for RB8E-13 (see Table 1) in which we aimed at equilibrating the melt composition with a CO_2 fluid in undersaturated conditions (initial CO_2 content = 8.8 wt.%), all the glass samples were synthesized under supersaturated conditions (initial CO_2 content > 30 wt.%).

The high-pressure experiments were performed in an end-loaded piston-cylinder apparatus in the 0.5 to 1.5 GPa pressure range. The temperature was set 1525°C to insure supraliquidus conditions. The temperatures were monitored by a WRe_3-WRe_{25} thermocouple in all experiments. The capsule was surrounded by an alumina sleeve to avoid contact with the graphite furnace.

A 19 mm talc-Pyrex assembly was used with a tapered graphite furnace to reduce the temperature gradient along the capsule (less than 20°C along the 12 mm Pt capsule). A pressure correction of 5% was applied for the talc pyrex assemblies consistent with the suggested friction correction (McDade et al., 2002) for talc-pyrex assemblies. Run durations were at least 1 hour to ensure equilibrium.

We used a special ¾ inch pressure plate with a special design in which holes have been drilled to improve the experimental quench rate (more than 200°C/s). Isobaric quenching ensured that quench (decompression) bubbles were not formed. Most of the recovered glasses are clear and crystal free; although in some samples, a small fraction of corundum (on the order of a few %) was identified in the ^{27}Al NMR spectrum. This corundum signal was also observed on a clear glass and we think the corundum signal arises from an external pollution coming from the outer alumina sleeve.

3. Analytical techniques:

153 *3.1 Electron Probe Micro-Analysis*

154 The major element compositions of glasses were determined using Electron Probe Micro-
155 Analyses (EPMA) on a Cameca SXFive©. The analytical conditions were 15kV and 10 nA
156 for voltage and current, respectively; and a 10 s peak counting time was used for each
157 element. Albite ($NaAlSi_3O_8$), alumina (Al_2O_3) and garnet ($Ca_3Al_2Si_3O_{12}$) were used as
158 standards for Na, Si, Al and Ca, respectively. Na was analyzed first. Analyses were conducted
159 in defocused mode (20 μm beam diameter) in order to reduce any elemental loss (Di Carlo et
160 al., 2006). The average major elements concentrations for the synthesized glasses were
161 obtained from more than 15 analyses. The determined glass composition is reported in Table
162 1 in wt.%. The standard deviation for each oxide does not exceed ±1 wt.%. From the major
163 element concentrations, it was then possible to calculate the degree of polymerization
164 expressed as the NBO/T and calculated on a stoichiometric basis (Mysen, 1988; see Table 1
165 and 2).

166

167 *3.2 Micro-Raman spectroscopy*

168 Micro-Raman spectra were acquired on a Jobin-Yvon Labram 300 spectrometer equipped
169 with an Innova 300-5W Argon ion laser from Coherent© operating at a wavelength of 514 nm
170 and on a Jobin-Yvon Labram HR800 equipped with a solid-state diode laser operating at 532
171 nm. The Labram 300 spectrometer is equipped with a 2400 grooves/mm grating allowing a
172 spectral resolution on the order of 1 cm^{-1}; Labram HR800 spectrometer is equipped with a
173 1800 grooves/mm grating allowing a spectral resolution on the order of 0.4 cm^{-1}. Analyses
174 were performed in confocal mode, using x50 Olympus objectives. The spectral range covered
175 was between 200 and 1250 cm^{-1}. The spectral frequency position was calibrated using the
176 emission lines of Ne- and Hg-lamps. On both spectrometers, the output power was set to 125

mW. Several spectra are collected on each sample. For each spectrum, we performed 10 scans on a given sample with an acquisition time of 5 to 10 s each on the Labram HR800 and 15 to 60 s on the Labram 300.

The CO_2 content in the recovered glass was determined by Raman spectroscopy using the deconvolution method proposed by Morizet et al. (2013) (details on the method are provided in the Supplementary material 1). For clarity, we provide the simulation of the Raman spectra in the Supplementary material 1 and the entire set of simulation results in Supplementary material 2. The determined CO_3/HF ratio corresponding to the ratio between the areas of the ν_1 CO_3^{2-} peak at ~1080 cm^{-1} and the areas of the silicate network high frequency envelop between 800 and 1050 cm^{-1} is reported in Table 1 and ranges from 0.45 and 1.33. It corresponds to a CO_2 solubility ranging from 6.0 to 18.0 wt.% for glass synthesized in between 0.5 and 1.5 GPa. Using the major element concentrations determined by EPMA provided in Table 1; we have calculated the corresponding CO_2 on a molar basis and expressed as the CO_2 molar fraction (XCO_2, see Table 1 and 2). For 6.0 to 18.0 wt.% CO_2, the XCO_2 varies between 0.086 to 0.234.

3.3 Micro-Fourier Transfrom Infra-Red spectroscopy

Micro-FTIR analyses were carried out on doubly-polished glass chips to determine the H_2O content. Analyses were conducted on a ThermoFisher FTIR5700 equipped with a Continuμm microscope. The spectrometer configuration was CaF_2 beamsplitter, and MCT-B detector and IR light to cover the 4000-6000 cm^{-1} spectral range. The concentration of OH^- (4500 cm^{-1}) and H_2O^{mol} (5200 cm^{-1}) was determined with the Beer-Lambert law (Ohlhorst et al., 2001). We used density values calculated from the chemical composition with the model of Lange and Carmichael (1990) which includes the change in oxides partial molar volume as a

function of pressure and temperature. Although this density model calculation is applied for liquid; recent work (Guillot and Sator, 2007) showed that the change in density in between liquid and glass is small (~10% in relative) towards an increase in density from the liquid to the glass. Therefore, the derived H_2O content with Beer-Lambert law will represent a maximum. As the OH^- and H_2O^{mol} extinction coefficient values are a strong function of the glass chemical composition, it was not possible to use an appropriate extinction coefficient value for the presently synthesized silicate glasses. We used the linear extinction coefficient applied to Alban Hill phonotephritic glass provided by Behrens et al. (2009): $\sigma OH = 0.62$ $L.mol^{-1}.cm^{-1}$ and $\sigma H_2O^{mol} = 1.02$ $L.mol^{-1}.cm^{-1}$. We choose those extinction coefficients as they were applied to glass compositions which are close to the ones studied here. The H_2O^{tot} is the sum of the OH and H_2O^{mol} concentrations. The H_2O^{tot} ranges from 0.5 to 2.8 wt.% with a typical error better than 0.2 wt.%. Except for RB8E-8 loaded with 6.9 wt.% H_2O, the presence of water is due to adsorption of atmospheric H_2O onto the starting material prior capsule preparation and sealing. Considering the high CO_2 solubility, the presence of H_2O does not play a crucial role on the measured CO_2 solubility in such depolymerized compositions (Xue and Kanzaki, 2004; Moussallam et al., 2016).

3.4 ^{17}O and ^{29}Si MAS NMR spectroscopy

We have measured the change in the degree of polymerization as a function of CO_2 content using ^{29}Si and ^{17}O MAS NMR spectroscopies (see Table 2). Solid State ^{17}O and ^{29}Si MAS NMR were performed with a Bruker Avance III 500 MHz spectrometer. The ^{17}O and ^{29}Si spectra were referenced against liquid H_2O at 0 ppm and TMS (Tetramethylsilane) at 0 ppm, respectively.

The ^{17}O MAS NMR spectra were acquired with a 2.5 mm CP/MAS probe and a MAS frequency of 30 kHz. We used a full shifted echo acquisition ($\pi/12$-τ-$\pi/6$-acq) sequence with a pulse length of 1 µs for the $\pi/12$ pulse. The delay τ was set to 1.13 ms (rotor-synchronized). A recycle delay between scans of 2 s was determined to be sufficient to insure complete relaxation of the ^{17}O spins. ^{29}Si-MAS NMR spectra were acquired with single $\pi/2$ excitation of 4 µs at a MAS frequency of 10 kHz. ^{29}Si-species can have long spin lattice relaxation time T1 in silicate glasses (Maekawa et al., 1991). A recycle delay of 120 s was shown to be sufficient for quantitative purpose. The spectra deconvolution was conducted with the DMFit2015 software (Massiot et al., 2002).

3.5 Differential Scanning Calorimetry

An indirect measurement of the melt viscosity in the CO_2-bearing glass was achieved by determining the glass transition temperature using Differential Scanning Calorimetry (DSC). One definition of the glass transition temperature is the temperature at which the $\log \eta = 12$ (Moynihan, 1995; Dingwell, 1995). The DSC measurements were conducted conjointly with thermogravimetric analyzer (ATG) in order to monitor weight loss during heating.

The glass samples were crushed to avoid sample fragmentation during the DSC experiment. The crushed glass was placed in one of the crucibles and its heat flow was measured. All measurements were performed with the same two crucibles under a constant flow of Ar gas of 20 $ml.min^{-1}$. Each sample was heated from 40°C across the glass transition at a rate of 20 K/min. An effective viscosity of 10^{12} Pa.s is usually achieved with a heating rate of 5 K/min (Webb and Knoche, 1996; Russell and Giordano, 2005).Using a faster heating rate (20 K/min) will lead to higher temperature for the definition of the onset peak and hence a corresponding lower viscosity than 10^{12} Pa.s. However, we used the same heating rate for all the analyzed

samples and the derived Tg could be compared in relative. We used Differential Scanning Calorimeter (DSC SETSYS EVO 2400) equipped with a thermogravimetric analyser (TGA) to determine the glass transition temperature (Tg) for four recovered glass samples (RB8-1, -2 and RB8E-3, -6). The DSC measurements determined the variation of heat flow (in mW) with increasing temperature. The calibration of the DSC was achieved by measuring the heat flow from two identical empty Pt-Rh crucibles (6 mm in diameter). The temperature calibration of the DSC apparatus was conducted by measuring the enthalpy of fusion of metal standards (gold, silver, aluminium and nickel). The baseline from the apparatus was subtracted from the standard and sample measurements. The DSC was then calibrated by measuring the enthalpy of fusion of metal standards (gold, silver, aluminium and nickel) and the sensitivity is better than 0.5% in relative with respect to the temperature measurement. Additional TGA measurements were also conducted conjointly to DSC measurements in order to determine the possible volatile loss during the heating. For RB8E-6, the TGA measurement was not conducted.

4. Results:

4.1 ^{17}O and ^{29}Si NMR spectra as a function of CO_2 content:

^{29}Si and ^{17}O MAS NMR spectra are shown in Figure 1. We conducted ^{29}Si MAS NMR spectra deconvolutions using three Gaussian lines (Figure 1A). Interpretation and assignment of the ^{29}Si spectrum simulation is complicated by the fact that there is only a single asymmetric peak resulting from the overlapping of several individual structural units (Q^n). However, it is commonly assumed that there is a structural equilibrium in between Q^n species (Stebbins, 1987; Maekawa et al., 1991; Mysen, 1999; Malfait et al., 2007a); such as:

271 $2Q^n \leftrightarrow Q^{n+1} + Q^{n-1}$ Eq. 2

272 The n values depend on the stoichiometric NBO/T of the melt. Here n = 2 for the glass
273 composition with NBO/T ~ 2. Hence, there is equilibrium in between Q^2, Q^3 and Q^1. The
274 derived peak positions (-76.3, -81.9 and -88.3 ppm for Q^1, Q^2 and Q^3, respectively) are
275 consistent with previous work (Engelhardt et al., 1985; Murdoch et al., 1985; Maekawa et al.,
276 1991; Zhang et al., 1997). The apparent NBO/T can then be calculated from the molar
277 fraction of the different Q^n species. The present simulation model is simplified as there is no
278 distinction between the Si environments surrounded by various Al atoms (Q^nm(Al) where m
279 represents the number of Al atoms surrounding the Q^n species; Hiet et al., 2009; Morizet et
280 al., 2014b) and those species are distributed in the single Gaussian line corresponding to a Q^n
281 species. As a result, the shown deconvolution in Figure 1A induces inevitably a systematic
282 bias on the NBO/T subsequent determination.

283 The difficulty of interpretation inherent to the overlapping contributions in ^{29}Si NMR spectra
284 is not present in the ^{17}O NMR spectra and the degree of polymerization is readily extracted
285 from the ^{17}O NMR spectra decomposition. ^{17}O MAS NMR spectrum line shape consists in
286 two main lines close to Gaussian shape due to the limited effect of second order quadrupolar
287 contribution (Kelsey et al., 2008). In agreement with Stebbins et al. (1997), each line at ~+100
288 ppm and ~+40 ppm in chemical shift is attributed to oxygen environments in NBO
289 configuration in the vicinity of Ca atoms (Ca-NBO) and to oxygen environments in BO
290 configuration (i.e. Si-O^{BO}-T with T = Si or Al), respectively. Two additional contributions are
291 also observed at ~-25 and +150 ppm and are attributed to the ^{17}O signature in oxygen
292 triclusters (O^{III}) and CO_3^{2-} environments (Morizet et al., *subm.*). The existence of O^{III}
293 (threefold coordinated O atom) is postulated in silicate glasses (Stebbins et al., 2001; Toplis et
294 al., 1997; Benoit et al., 2005; Iuga et al., 2005; Thompson et al., 2011) at ^{17}O chemical shift

close to the BO ^{17}O chemical shift. We did not identify possible contribution from free oxygens which have been inferred in silicate melt from previous studies (Nesbitt et al., 2015; Sawyer et al., 2015). The exact position of this contribution in the ^{17}O NMR spectrum is not clear and would overlap with oxygen signal in NBO configuration (Nasikas et al., 2012). Furthermore, in the present investigated silicate melt composition (SiO_2 > 50 mol.%), the abundance of free O^{2-} anions is expected to be extremely low (<4% of the total oxygen; Nesbitt et al., 2015).

4.2 Glass transition temperature determination

We show in Figure 2 the change in the heat flow as a function of the temperature; except for RB8E-6 the thermogravimetric changes (ATG) are also reported in mg as a function of temperature. There is a constant decrease in the heat flow followed by an increase above 600°C. This abrupt change in the heat flow curve shape with increasing temperature may be attributed to crystallization of the sample. The increase in the heat flow is also accompanied by a brutal change in the ATG curve indicating a substantial loss in the sample mass. This important loss might be attributed probable CO_2 diffusion out of the sample. Recovered samples exhibit large bubbled aspect suggesting an efficient CO_2 degassing. Anyhow, this process occurs well-above the glass transition temperature. The comparison of the heat flow and ATG curves in the vicinity of Tg does not indicate mass loss; hence the determined Tg reflects the effective glass transition temperature for the CO_2-bearing glass sample.

In DSC measurements, the Tg determination is done by the in-built DSC software (Setsoft 2000) using the three points definition. Two tangents with identical slope are fitted prior and after the supposed glass transition region. A third tangent is then fitted in the glass transition region and Tg is defined as the mid-point of the third tangent in between the two parallel

tangents (Morizet et al., 2015a). DSC measurements result in a typical error on the order of ±10 K for the Tg determination (Morizet et al., 2015a); however, some studies reported a lower error ±2.5 K (Giordano et al., 2005; Morizet et al., 2007). Considering an error of ±10 K does not induce any change in the outcome of the present work. For the four measured samples, we observe a change in Tg from 475 to 571°C for RB8-1 and RB8E-6, respectively. Hence, the observed variation in Tg is far above the potential error. Meanwhile, it should be pointed out that for two samples (RB8-1 and RB8E-3) having similar 1) CO_2 content (~17 wt.% CO_2), 2) similar degree of polymerization (1.9 and 2.1, respectively), we observe a difference of 38°C in Tg value. Such a difference can be due to slight change in the glass chemical composition inducing a change in Tg value.

5. Discussion:

5.1 Change in silicate glass polymerization as a function of CO_2 content from ^{17}O and ^{29}Si NMR

In the present work, we investigated the change in the degree of polymerization for CO_2-bearing silicate glasses using both ^{29}Si and ^{17}O NMR results with the subsequent simulations (^{29}Si and ^{17}O) shown in Figure 1. We consider the deviation in the degree of polymerization (DDP) which corresponds to the ratio between the NBO/T determined from ^{17}O and ^{29}Si NMR spectroscopy and the NBO/T calculated from the stoichiometric chemical composition determined by EPMA (see Table 1). Using the DDP instead of the NBO/T has the advantage to average out any potential major element composition heterogeneities (see Table 1). However, we also provide in the Supplementary material plots showing the non-normalized change in the NBO/T as determined from ^{29}Si and ^{17}O NMR spectroscopy as a function of XCO_2. We show in Figure 3 the DDP as a function of XCO_2 for 1) the CO_2 dissolution model

343 of Eq. 1, 2) the decomposition of ^{29}Si NMR spectra and 3) the decomposition of ^{17}O NMR
344 spectra. We observe that the change in the DDP from ^{29}Si and ^{17}O NMR spectra is linearly
345 correlated to the CO_2 content. Both results show that increasing XCO_2 induces a strong
346 increase in the degree of polymerization (i.e. decreasing DDP with increasing XCO_2)
347 confirming the recent work (Morizet et al., 2014b; Moussallam et al., 2016) for strongly
348 silica-undersaturated melt compositions and therefore extending the observation to a large
349 variety of silicate melt chemical composition.

350 This result has a major implication as it tends to endorse the chemical model of Eq. 1 for CO_2
351 dissolution. Consequently, in accordance to Eq. 1, CO_2 molecules mainly dissolve in silicate
352 melt structure as Free Ionic Carbonate $M^{n+}..CO_3^{2-}$ groups (FIC) as proposed by recent works
353 (Moussallam et al., 2016; Morizet et al., 2015b). For the studied composition, the FIC are
354 mainly $Ca^{2+}..CO_3^{2-}$. The presence of FIC also indicates that a carbonate subnetwork is
355 coexisting with a silicate subnetwork. Both are intimately linked; however, as suggested in
356 recent study (Morizet et al., 2014a) for alkali-rich melt composition, the FIC represents the
357 precursor of the two liquids immiscibility (carbonate liquid and silicate liquid) process often
358 invoked to explain the coexistence of CO_2-rich silicate rocks and carbonatites (Mitchell, 2005;
359 Brooker and Kjarsgaard, 2011; Sharygin et al., 2012; Russell et al., 2012).

360 Although we do not have data points for $XCO_2 < 0.086$, for both ^{29}Si and ^{17}O NMR, we
361 expect that CO_2 does not influence the degree of polymerization possibly because of another
362 unidentified CO_2 dissolution mechanism. This would also be consistent with the recent results
363 of Sifré et al. (2014) showing that the silicate melt electrical conductivity is not affected up to
364 6 wt.% CO_2. Until we fulfil this lack of data, it seems that the trend at $XCO_2 = 0$ could extend
365 at NBO/T ratio > 1 suggesting an excess in NBOs concentration. The excess in NBOs has
366 been identified in polymerized CaO-Al_2O_3-SiO_2 silicate glasses (Benoit et al., 2005; Stebbins
367 and Xu, 1997) but never reported for more depolymerized compositions.

We observe a slight mismatch (10% difference) in between the ^{29}Si and ^{17}O NMR results: the ^{29}Si NMR results show a lower DDP than in ^{17}O NMR results. Although the ^{29}Si simulation approach is simplified, it appears that both ^{17}O and ^{29}Si NMR results are consistent. Hence, the ^{29}Si NMR results can be used to quantify the effect CO_2 produces on the degree of silicate melt polymerization. Furthermore, it can be used to establish a clear CO_2 dissolution mechanism reaction for the studied composition.

5.2 CO_2 dissolution mechanism reaction in silicate undersaturated glass composition

The DDP as a function of CO_2 content obtained by NMR strongly deviates from the chemical model of Eq. 1 (*red line* in Figure 3) suggesting that there is a much more important change in NBO/T than the suggested change by Eq. 1. This implies that CO_2 has a much stronger effect on the silicate melt degree of polymerization than suggested. Serendipitously, we interpret this discrepancy by the fact that the CO_2 dissolution mechanism does not strictly follow the mole-to-mole basis changes of Eq. 1. A more complex mechanism is possible where network modifying cations (mostly Ca^{2+} in here) in silicate melt/glass share their positive charges with several oxygen negative charges (Allwardt and Stebbins, 2004; Benoit et al., 2005; Mountjoy, 2007) and consequently throughout multiple weak bonding in the silicate network. Considering that ^{29}Si and ^{17}O NMR results in Figure 3 show a comparable evolution; the Q^n species distribution as a function of CO_2 content can be extracted from ^{29}Si NMR results. We used ^{29}Si NMR results to propose the CO_2 dissolution mechanism represented by Eq. 3.This mechanism reproduces adequately the change in Q^n speciation shown in Figure 4 and the increase in the degree of polymerization (Figure 3) for the currently investigated composition:

$$2.25CO_2^{fluid} + \frac{7.5}{2}Ca^{2+} + 2.5Q^{1\,melt} \leftrightarrow 2.25Ca^{2+}..CO_3^{2-\,melt} + 0.5Q^{2\,melt} + 2.0Q^{3\,melt} + \frac{3.0}{2}Ca^{2+}$$

Eq. 3

In this equation, Q^1 species transform into Q^2 species in agreement with Eq. 1 but it also transforms into Q^3 species. The stoichiometric coefficients in front of each Q^n species correspond to the slope of the linear regressions determined in Figure 4 for the evolution of each Q^n species: -2.5, +0.5 and +2.0 for Q^1, Q^2 and Q^3, respectively. The number of involved Ca^{2+} is fixed by the total negative charge carried by the Q^1 species: 2.5 x 3 = 7.5. The same applies on the right hand side of the chemical reaction: 2.0 x 1 + 0.5 x 2 = 3.0. Hence, the excess Ca^{2+} (7.5/2 – 3.0/2 = 4.5/2) is compensated by CO_3^{2-} to form FIC $Ca^{2+}..CO_3^{2-}$ in the melt structure. Hence, the number of FIC $Ca^{2+}..CO_3^{2-}$ formed fixes the number of CO_2 molecules incorporated from the fluid phase into the melt structure.

5.3 Implication on the effect of CO_2 on silicate melt viscosity: A preliminary model

The conventional view of the relationship in between the melt structure and the corresponding melt physical properties is to consider that an increase in melt polymerization induces an increase in melt viscosity (Mysen, 1998; Giordano et al., 2008; Moussallam et al., 2016; Stebbins, 2016). Hence, the presented NMR results in Figure 3 are by extension in favor for this increase in melt viscosity with increasing CO_2 content.

For several glass samples (6.0 and 17.1 wt.% CO_2), we have determined the glass transition temperature (Tg), which represents a proxy of the melt viscosity (log η = 12; Moynihan, 1995; Dingwell, 1995; Webb and Knoche, 1996). Tg was measured at 571 and 475 ±5°C for 6.2 and 17.1 wt.% CO_2 glass samples, respectively. As shown in Figure 5, compositions with the more polymerization (i.e. lower CO_2 content) have lower value of Tg. This result is in

413 stark contrast with our current knowledge on the link between the silicate melt molecular
414 structure and the corresponding silicate melt physical properties. As indicated in Figure 5, the
415 increase in polymerization is accompanied by a decrease in melt viscosity which is
416 counterintuitive and in opposition to what is currently accepted.

417 The discrepancy between spectroscopic observations and physical measurements observed in
418 Figure 5 has a major implication. Indeed, we show in the present work that quantification in
419 the silicate network changes upon CO_2 dissolution using spectroscopic methods cannot be
420 straightforwardly related to a corresponding change in melt physical properties since an
421 increase in silicate network polymerization implies an increase in viscosity. This contrasts
422 with studies on H_2O dissolution in silicate melt showing that both the silicate melt structure
423 and the physical properties are strongly correlated (Richet, 1984; Dingwell et al., 1996; Richet
424 et al., 1996; Giordano et al., 2008). Mantle melts, particularly rich in CO_2 such as melilitites
425 and kimberlites, therefore seem more complex than the conventional silicate melts in their
426 structure-properties relationships.

427 We propose a possible reconciliation of the spectroscopic results and physical measurements.
428 We have shown in Eq. 3 that CO_2 dissolves in silicate melt structure by forming FIC groups
429 (i.e. $Ca^{2+}..CO_3^{2-}$). Our proposition is that FIC clusters forming an individual carbonate
430 subnetwork along a silicate melt subnetwork behave in a similar way to a carbonate liquid
431 (Kono et al., 2014; Vuilleumier et al., 2015). Therefore upon CO_2 dissolution, the molten
432 system is an intimate mixture (i.e. two interacting liquids) of a silicate melt and a carbonate
433 melt. With increasing CO_2 dissolution, the silicate melt is progressively diluted by a carbonate
434 melt having an extremely low viscosity as demonstrated by Kono et al. (2014). The viscosity
435 of the silicate melt subnetwork increases due to the fact that CO_2 induces a polymerization of
436 the Q^n species (see Eq. 3 and Figure 3) but this increase in viscosity is counterbalanced by the
437 progressive increase in the carbonate melt subnetwork of extremely low viscosity. Hence, the

progressive CO_2 dissolution in a silicate melt induces a decrease in melt viscosity therefore explaining the extremely low viscosity of CO_2-rich deep mantle magmatic liquids such as kimberlites.

We propose a model for silicate melt viscosity change as a function of CO_2 content. We should emphasize that the proposed scenario is preliminary and needs to be confirmed in the future by experimental investigations. To establish this model we started with the following hypothesis: in presence of CO_2, the system is an intimate mixture between a silicate melt and a carbonate melt with each melt having its own viscosity properties. Hence, the entire system viscosity can be approximated by a linear combination of viscosity as suggested by chemical science studies (Mialkowski et al., 2002; Chagnes et al., 2004; Ye et al., 2016) such as:

$$\eta_{SL+CL} = X_{SL}\eta_{SL} + X_{CL}\eta_{CL} \qquad \text{Eq. 4}$$

Where η_{SL}, η_{CL} and η_{SL+CL} correspond to the viscosity of the silicate liquid, carbonate liquid and the mixture of both liquids, respectively. X_{SL} and X_{CL} correspond to the molar fraction of the silicate and carbonate liquid, respectively. We considered a constant viscosity value for the carbonate liquid given by Kono et al. (2014): $\log \eta_{CL} = -2.21$ Pa.s. This value is independent of pressure and has been determined at 1750 K by Kono et al. (2014). The X_{CL} is given by the molar fraction of the dissolved CO_2 (XCO_2 in Table 1). Hence, the silicate melt molar fraction can be calculated such as $X_{SL} = 1 - X_{CL}$.

In order to calculate the η_{SL} we considered that when CO_2 molecule dissolves in the system, it withdraws one Ca^{2+} cation and one O^{2-} anion to form FIC $Ca^{2+}..CO_3^{2-}$. Hence, the silicate liquid composition changes at each XCO_2 due to the withdrawing of the Ca^{2+} cation. The silicate liquid composition is therefore recalculated at each XCO_2 such as:

$$X_{SL}^{CaO} = X_{SL}^{CaO\ Init.} - X_{CO_2} \qquad \text{Eq. 5}$$

461 In Eq. 5, $X_{SL}^{CaO\ Init.}$ represents the initial CaO molar fraction in the silicate melt composition
462 and is 0.531 calculated from the volatile-free theoretical composition reported in Table 1. We
463 used the viscosity model proposed by Giordano and Russell (2007) to calculate the silicate
464 liquid viscosity. Calculation was conducted at 1750 K so as to match the carbonate liquid
465 viscosity value proposed by Kono et al. (2014). We did not take into account the effect of
466 pressure on the viscosity of the silicate liquid as in the interval 0.5-1.5 GPa the change in
467 silicate melt viscosity is likely to be negligible (Allwardt et al., 2007). Under these conditions,
468 the $\log \eta_{SL\ Init.} = -0.32$ Pa.s for the RB8 theoretical composition reported in Table 1.

469 The calculation results are shown in Figure 6; the corresponding calculations are provided in
470 the Supplementary material 2 as a spreadsheet. We have reported the calculation in three
471 different cases. The η_{SL} represents the change in viscosity of the silicate liquid determined
472 with the model of Giordano and Russel (2007) and taking into account the changes in silicate
473 liquid composition (i.e. Eq. 5). The $X_{SL}\eta_{SL\ Init.} + X_{CL}\eta_{CL}$ represents the change in viscosity of
474 the two liquid mixtures considering a constant viscosity for the silicate liquid at $\log \eta_{SL\ Init.} = -$
475 0.32 Pa.s and calculated for the theoretical composition using the model of Giordano and
476 Russell (2007). The proportion of each liquid is progressively changed with increasing XCO_2.
477 The third curve $X_{SL}\eta_{SL} + X_{CL}\eta_{CL}$ corresponds to the change in viscosity of the two liquid
478 mixtures as proposed in Eq. 4. The calculation includes the effect of the progressive
479 enrichment in the carbonate liquid and the progressive Ca depletion in the silicate liquid.

480 As shown in Figure 6, the viscosity of the silicate liquid increases with CO_2 content due to the
481 progressive Ca depletion (i.e. SiO_2 increase). For a constant silicate liquid viscosity, the
482 increase in carbonate liquid proportion induces a linear decrease in the viscosity of the two
483 liquid mixtures. The combination of the different effects show that the viscosity of the two
484 liquid mixtures is almost not affected or only slightly decreasing; in other words, the presence
485 of CO_2 does not induce a dramatic effect on the viscosity of the two liquid mixtures. The

calculations conducted at 1600 K produce similar results with only a slight decrease in viscosity of the two liquid mixtures (see Supplementary material 2). For fully polymerized compositions, Brearley and Montana (1989) and White and Montana (1990) suggested a decreasing effect of CO_2 on silicate melt viscosity. Bourgue and Richet (2001) proposed a decrease in silicate melt viscosity with increasing CO_2 content. Morizet et al. (2007) pointed out the absence of effect of CO_2 on viscosity for phonolitic and jadeitic silicate melt compositions. The model calculation results suggest that the addition of CO_2 to a silicate melt induces negligible effect on the viscosity or a slight decrease in melt viscosity. Although there is a strong increase in silicate melt polymerization, the interplay between a carbonate liquid and a silicate liquid counterbalances the increase in the silicate melt viscosity and the viscosity of the two liquid mixtures is slightly decreasing with increasing CO_2 content.

In an immiscible process between a silicate liquid and a carbonate liquid, the exsolution of the carbonate liquid would provoke the silicate liquid to be stalled in depth due to its high viscosity.

6. Summary:

For silica undersaturated melt composition equivalent to melilitite lava composition, using ^{17}O and ^{29}Si NMR spectroscopy, we have shown that increasing CO_2 content induces the polymerization of the silicate network structure. This polymerization involves the formation of Free Ionic Carbonate such as $Ca^{2+}..CO_3^{2-}$ which constitutes a carbonate subnetwork linked to the silicate subnetwork. However, such dissolution mechanism does not proceed on a mole-to-mole basis and a more complex mechanism is to be considered. We used the Q^n distribution determined by ^{29}Si NMR to constrain the CO_2 dissolution mechanism and showed that the polymerization is much stronger than proposed by chemical models. We derived a

chemical reaction for the CO_2 dissolution which could be applied to a large variety of low silica melt such as kimberlites.

If the increasing polymerization with increasing CO_2 content points towards an increase in melt viscosity, glass transition temperature changes negatively with increasing CO_2 content suggesting a negative effect of CO_2 on melt viscosity. This inconsistency can be reconciled considering that the silicate subnetwork (high viscosity) is progressively diluted by a carbonate subnetwork having an extremely low viscosity. Hence, the viscosity of the two liquid mixtures is not increasing but decreasing instead. This mechanism would explain the fast ascent rate of CO_2-rich kimberlitic melt. The strong buoyancy and rapid ascent of the kimberlitic melt will be ensured by the existence of a CO_2-rich fluid phase created upon decompression through the ascent but also because the viscosity is kept low in the two liquid mixtures configuration.

Acknowledgements

The authors are grateful to the ANR agency which financed the current work through the ANR-2010-BLAN-621 “Electrolith”. The authors would like to thank the European Research Council who partly funded this work through the ERC project grant number 279790. The authors thank the University of Orléans, the University of Nantes and the CNRS for their access to analytical facilities

References

Allwardt, J.R., Stebbins, J.F., 2004. Ca-Mg and K-Mg mixing around non-bridging O atoms in silicate glasses: an investigation using ^{17}O MAS and 3QMAS NMR. Am. Mineral. 89, 777–784.

Allwardt, J.R., Stebbins, J. F., Terasaki, H., Du, L.-S., Frost, D.J., Withers, A.C., Hirschmann, M.M., Suzuki, A., Ohtani, E., 2007. Effect of structural transitions on properties of high pressure silicate melts: ^{27}Al NMR, glass densities, and melt viscosities. Am. Mineral. 92, 1093–1104.

Behrens, H., Misiti, V., Freda, C., Vetere, F., Botcharnikov, R.E. , Scarlato, P., 2009 Solubility of H_2O and CO_2 in ultrapotassic melts at 1200 and 1250 °C and pressure from 50 to 500 MPa. Am. Mineral. 94, 105–120.

Benoit, M., Profeta, M., Mauri, F., Pickard, C.J., Tuckerman, M.E., 2005. First-principles calculation of the ^{17}O NMR parameters of a calcium aluminosilicate glass. J. Phys. Chem. B 109, 6052–6060.

Bosshardt-Stadlin, S.A. , Mattsson, H.B., Keller, J., 2014. Magma mixing and forced exsolution of CO_2 during the explosive 2007–2008 eruption of Oldoinyo Lengai (Tanzania). J. Volc. Geotherm. Res. 285, 229–246.

Brearley, M., Montana, A., 1989. The effect of CO_2 on the viscosity of silicate liquids at high pressure. Geohim. Cosmochim. Acta 53, 2609–2616.

Brooker, R.A., Kjarsgaard, B.A., 2011. Silicate–carbonate liquid immiscibility and phase relations in the system SiO_2–Na_2O–Al_2O_3–CaO–CO_2 at 0.1–2.5 GPa with applications to carbonatite genesis. J. Petrol. 52, 1281–1305.

552 Brooker, R.A., Kohn, S.C., Holloway, J.R., McMillan, P.F., 2001. Structural controls on the
553 solubility of CO_2 in silicate melts. Part II: IR characteristics of carbonate groups in silicate
554 glasses. Chem. Geol. 174, 241–254.

555 Chagnes, A., Tougui, A., Carré, B., Ranganathan, N., Lemordant, D., 2004. Abnormal
556 temperature dependence of the viscosity of Ethylammonium Nitrate-Methanol ionic mixtures.
557 J. Sol. Chem. 33, 247–255.

558 Dasgupta, R., Hirschmann, M.M., 2006. Melting in the Earth's deep upper mantle caused by
559 carbon dioxide. Nature 440, 659–662.

560 Dasgupta, R., 2013. Ingassing, storage, and outgassing of terrestrial carbon through geologic
561 time. Rev. Mineral. Geochem. 75, 183–229.

562 Di Carlo, I., Pichavant, M., Rotolo, S.G., Scaillet, B., 2006. Experimental crystallization of a
563 high-K arc basalt: the golden pumice, Stromboli volcano (Italy). J. Petrol. 47, 1317–1343.

564 Dingwell, D.B., 1995. Relaxation in silicate melts: some applications. In: Stebbins, J.F.,
565 McMillan, P.F., Dingwell, D.B. (Eds.), Structure, Dynamics and Properties of Silicate Melts.
566 Washington, Mineralogical Society of America, Geochemical Society, Reviews in
567 Mineralogy 32, pp. 21–66.

568 Dingwell, D.B., Romano, C., Hess, K.-U., 1996. The effect of water on the viscosity of a
569 haplogranitic melt under P-T-X conditions relevant to silicic volcanism. Contrib. Mineral.
570 Petrol. 124, 19–28.

571 Eggler, D.H., 1978. The effect of CO_2 upon partial melting of peridotite in the system Na_2O–
572 CaO–Al_2O_3–MgO–SiO_2–CO_2 to 35kb, with an analysis of melting in a peridotite-H_2O–CO_2
573 system. Am. J. Sci. 278, 305–343.

574 Engelhardt, G., Nofz, M., Forkel, K., Wihsmann, F.G., Magi, M., Samoson, A., Lippmaa, E.,
575 1985. Structural studies of calcium aluminosilicate glasses by high-resolution solid-state ^{29}Si
576 and ^{27}Al magic angle spinning nuclear magnetic resonance. Phys. Chem. Glasses 26, 157–
577 165.

578 Farnan, I., Grandinetti, P.J., Baltisberger, J.H., Stebbins, J.F., Werner, U., Eastman, M.A.,
579 Pines, A., 1992. Quantification of the disorder in network-modified silicate glasses. Nature
580 358, 31–35.

581 Giordano, D., Russell, J.K., 2007. A rheological model for glassforming silicate melts in the
582 systems CAS, MAS, MCAS. J. Phys. Condens. Matter 19, 255148–255159.

583 Giordano, D., Russell, J.K., Dingwell, D.B., 2008. Viscosity of magmatic liquids: a model.
584 Earth Planet. Science Lett. 271, 123–134.

585 Guillot, B., Sator, N., 2007. A computer simulation study of natural silicate melts. Part II:
586 high pressure properties. Geochim. et Cosmochim. Acta 71, 4538–4556.

587 Hiet, J., Deschamps, M., Pellerin, N., Fayon, F., Massiot, D., 2009. Probing chemical disorder
588 in glasses using silicon-29 NMR spectral editing. Phys. Chem. Chem. Phys. 11, 6935–6940.

589 Iuga, D., Morais, C., Gan, Z., Neuville, D.R., Cormier, L., Massiot, D., 2005. NMR
590 Heteronuclear Correlation between quadrupolar nuclei in solids. J. Am. Chem. Soc. 127,
591 11540–11541.

592 Kelsey, K.E., Allwardt, J.R., Stebbins, J.F., 2008. Ca-Mg mixing in aluminosilicate glasses:
593 An investigation using the ^{17}O MAS and 3QMAS and ^{27}Al MAS NMR. J. Non-Cryst. Solids
594 354, 4644–4653.

595 Kono, Y., Kenney-Benson, C., Hummer, D., Ohfuji, H., Park, C., Shen, G., Wang, Y.,
596 Kavner, A., Manning, C.E., 2014. Ultralow viscosity of carbonate melts at high pressures.
597 Nature Comm 5, DOI: 10.1038/ncomms6091.

598 Lange, R., Carmichael, I.S.E., 1990. Thermodynamic properties of silicate liquids with
599 emphasis on density, thermal expansion and compressibility. In J. Nicholls and J.K. Russell,
600 Eds., Modern Methods of Igneous Petrology: Understanding Magmatic Processes, 24, p. 25–
601 64. Reviews in Mineralogy, Mineralogical Society of America, Chantilly, Virginia.

602 Lee, S.K., 2004. Structure of silicate glasses and melts at high pressure: Quantum chemical
603 calculations and Solid-State NMR. J. Phys. Chem. B 108, 5889-5900.

604 Lee, S.K., 2005. Microscopic origins of macroscopic properties of silicate melts and glasses at
605 ambient and high pressure: Implications for melt generation and dynamics. Geochim. et
606 Cosmochim. Acta 69, 3695–3710.

607 Lee, S.K., Stebbins, J.F., 2009. Effects of the degree of polymerization on the structure of
608 sodium silicate and aluminosilicate glasses and melts: An ^{17}O NMR study. Geochim. et
609 Cosmochim. Acta 73, 1109–1119.

610 Maekawa, H., Maekawa, T., Kawamura, K., Yokokawa, T., 1991. The structural groups of
611 alkali silicate glasses determined from ^{29}Si MAS NMR. J. Non-Cryst. Solids 127, 53–64.

612 Malfait, W.J., Zakaznova-Herzog, V.P. , Halter, W.E., 2007. Quantitative Raman
613 spectroscopy: high-temperature speciation of potassium silicate melts. J. Non-Cryst. Solids
614 doi:10.1016/j.jnoncrysol.2007.06.031.

615 Massiot, D., Fayon, F., Capron, M., King, I., Le Calvé, S., Alonso, B., Durand, J.O., Bujoli,
616 B., Gan, Z., Hoatson, G., 2002. Modelling one and two-dimensional solid-state NMR spectra.
617 Magn. Reson. Chem. 40, 70–76.

618 Massiot, D., Messinger, R.J., Cadars, S., Deschamps, M., Montouillout, V., Pellerin, N.,
619 Veron, E., Allix, M., Florian, P., Fayon, F., 2013. Topological, geometric, and chemical order
620 in materials: Insights from Solid-State NMR. Acc. Chem. Res. 46, 1975–1984.

621 Massuyeau, M., Gardès, E., Morizet, Y., Gaillard, F., 2015. A model for the activity of silica
622 along the carbonatite-kimberlite-melilitite-basanite melt compositional joint. Chem. Geol.
623 418, 206–216.

624 McDade, P., Wood, B.J., Van Westrenen, W., Brooker, R.A., Gudmundsson, G., Soulard, H.,
625 Najorka, J., Blundy, J., 2002. Pressure corrections for a selection of piston–cylinder cell
626 assemblies. Min. Mag. 66, 1021–1028.

627 Mialkowski, C., Chagnes, A., Carré, A., Lemordant, D., Willmann, P., 2002. Excess
628 thermodynamic properties of binary liquid mixtures containing dimethylcarbonate and γ-
629 butyrolactone. J. Chem. Thermo. 34, 1847-1856.

630 Mitchell, R.H., 2005. Carbonatites and carbonatites and carbonatites. Can. Mineral. 43, 2049–
631 2068.

632 Morizet, Y., Nichols, A.R.L., Kohn, S.C., Brooker, R.A., Dingwell, D.B., 2007. The influence
633 of H_2O and CO_2 on the glass transition temperature: insights into the effects of volatiles on
634 magma viscosity. Eur. J. Mineral. 19, 657–669.

635 Morizet, Y., Brooker, R.A., Iacono-Marziano, G., Kjarsgaard, B., 2013. Quantification of CO_2
636 dissolved in silicate glasses of various compositions with Micro-Raman spectroscopy. Am.
637 Mineral. 98, 1788–1802.

638 Morizet, Y., Paris, M., Gaillard, F., Scaillet, B., 2014a. Carbon dioxide in silica-
639 undersaturated melt. Part I: The effect of mixed alkalis (K and Na) on CO_2 solubility and
640 speciation. Geochim. et Cosmochim. Acta 141, 45–61.

641 Morizet, Y., Paris, M., Gaillard, F., Scaillet, B., 2014b. Carbon dioxide in silica-
642 undersaturated melt. Part I: the effect of mixed alkalis (K and Na) on CO_2 solubility and
643 speciation. Geochim. et Cosmochim. Acta 141, 45–61.

644 Morizet, Y., Ory, S., Di Carlo, I., Scaillet, B., Echegut, P., 2015a. The effect of Sulphur on the
645 glass transition temperature in anorthite-diopside eutectic glasses. Chem. Geol. 416, 11-18.

646 Morizet, Y., Vuilleumier, R., Paris, M., 2015b. A NMR and molecular dynamics study of
647 CO_2-bearing basaltic melts and glasses. Chem. Geol. 418, 89–103.

648 Morizet, Y., Paris, M., Sifré, D., Di Carlo, I., Gaillard, F.,2017. The effect of Mg
649 concentration in silicate glasses on CO_2 solubility and solution mechanism: Implication for
650 natural magmatic systems. Geochim. et Cosmochim. Acta, 198, 115-130.

651 Mountjoy, G., 2007. The local atomic environment of oxygen in silicate glasses from
652 molecular dynamics. J. Non-Cryst. Solids 353, 1849–1853.

653 Moussallam, Y., Florian, P., Corradini, D., Morizet, Y., Sator, N., Vuilleumier, R., Guillot,
654 B., Iacono-Marziano, G., Schmidt, B.C., Gaillard, F., 2016. The molecular structure of melts
655 along the carbonatite–kimberlite–basalt compositional joint: CO_2 and polymerization. Earth
656 Planet. Science Lett. 434, 129-140.

657 Moynihan, C.T., 1995. Relaxation in silicate melts: some applications. Rev. Mineral. 32, 1–
658 20.

659 Murdoch, J.B., Stebbins, J.F., Carmichael, I.S.E., 1985. High resolution ^{29}Si NMR study of
660 silicate and aluminosilicate glasses: the effect of network modifying cations. Am. Mineral. 70,
661 332–343.

662 Mysen, B.O., 1988. Structure and properties of silicate melts. Developments in Geochemistry
663 4. Elsevier. Amsterdam. 354p.

664 Mysen, B.O., 1998. Transport and configurational properties of silicate melts: Relationship to
665 melt structure at magmatic temperatures. Phys. Earth Planet. Int. 107, 23–32.

666 Mysen, B.O., 1999. Structure and properties of magmatic liquids: From haplobasalt to
667 haploandesite. Geochim. et Cosmochim. Acta 63, 95–112.

668 Mysen, B.O., Virgo, D., 1980a. Solubility mechanisms of carbon dioxide in silicate melts; a
669 Raman spectroscopic study. Am. Mineral. 65, 885–899.

670 Mysen, B.O., Virgo, D., 1980b. The solubility behavior of CO_2 in melts on the join
671 $NaAlSi_3O_8$–$CaAl_2Si_2O_8$–CO_2 at high pressures and temperatures; a Raman spectroscopic
672 study. Am. Mineral. 65, 1166–1175.

673 Nasikas, N.K., Edwards, T.G., Sen, S., Papatheodorou, G.N., 2012. Structural characteristics
674 of novel Ca-Mg orthosilicate and suborthosilicate glasses: Results from ^{29}Si and ^{17}O NMR
675 spectroscopy. J. Phys. Chem. B 116, 2696–2702.

676 Nesbitt, H.W., Bancroft, G.M., Henderson, G.S., Sawyer, R., Secco, R.A., 2015. Direct and
677 indirect evidence for free oxygen (O^{2-}) in MO-silicate glasses and melts (M = Mg, Ca, Pb).
678 Am. Mineral. 100, 2566-2578.

679 Ohlhorst, S., Behrens, H., Holtz, F., 2001. Compositional dependence of molar absorptivities
680 of near-infrared OH^- and H_2O bands in rhyolitic to basaltic glasses. Chem. Geol. 174, 5–20.

681 Richet, P., 1984. Viscosity and configurational entropy of silicate melts. Geochim. et
682 Cosmochim. Acta 48, 471–483.

683 Richet, P., Lejeune, A.-M., Holtz, F., Roux, J., 1996. Water and the viscosity of andesite
684 melts. Chem. Geol. 128, 185–197.

685 Russell, J.K., Giordano, D., 2005. A model for silicate melt viscosity in the system
686 $CaMgSi_2O_6$-$CaAl_2Si_2O_8$-$NaAlSi_3O_8$. Geochim. et Cosmochim. Acta 69, 5333-5349.

687 Russell, J.K., Porritt, L.A., Lavallée, Y., Dingwell, D.B., 2012. Kimberlite ascent by
688 assimilation-fuelled buoyancy. Nature 481, 352–356.

689 Sawyer, R., Nesbitt, H.W., Bancroft, G.M., Thibault, Y., Secco, R.A., 2015. Spectroscopic
690 studies of oxygen speciation in K-silicate glasses and melts. Can. J. Chem. 93, 60–73.

691 Schmidt, B.C., Riemer, T., Kohn, S.C., Behrens, H., Dupree, R., 2000. Different water
692 solubility mechanisms in hydrous glasses along the Qz-Ab Join: evidence from NMR
693 spectroscopy. Geochim. et Cosmochim. Acta 64, 513–526.

694 Sharygin, V.V., Kamenetsky, V.S., Zaitsev, A.N., Kamenetsky, M.B., 2012. Silicate–
695 natrocarbonatite liquid immiscibility in 1917 eruption combeite–wollastonite nephelinite,
696 Oldoinyo Lengai Volcano, Tanzania: Melt inclusion study. Lithos 152, 23-39.

697 Sifré, D., Gardès, E., Massuyeau, M., Hashim, L., Hier-Majumder, S., Gaillard, F., 2014.
698 Electrical conductivity during incipient melting in the oceanic low-velocity zone. Nature 509,
699 81–87.

700 Stebbins, J.F., 1987. Identification of multiple structural species in silicate glasses by ^{29}Si
701 NMR. Nature 330, 465–467.

702 Stebbins, J.F., 2016. Glass structure, melt structure, and dynamics: Some concepts for
703 petrology. Am. Mineral. 101, 753-768.

704 Stebbins, J.F., Xu, Z., 1997. NMR evidence for excess non-bridging oxygens in an
705 aluminosilicate glass. Nature 390, 60–62.

706 Stebbins, J.F., Oglesby, J.V., Xu, Z., 1997. Disorder among network-modifier cations in
707 silicate glasses: new constraints from triple-quantum ^{17}O NMR. Am. Mineral. 82, 1116–1124.

708 Stebbins, J.F., Oglesby, J.V., Kroeker, S., 2001. Oxygen triclusters in crystalline $CaAl_4O_7$
709 (grossite) and calcium aluminosilicate glasses: oxygen-17 NMR. Am. Mineral. 86, 1307–
710 1311.

711 Taylor, W.R., Green, D.H., 1988. Measurement of reduced peridotite–C–O–H solidus and
712 implications for redox melting of the mantle. Nature 332, 349–352.

713 Thompson, L.M., Stebbins, J.F., 2011. Non-bridging oxygen and high-coordinated aluminum
714 in metaluminous and peraluminous calcium and potassium aluminosilicate glasses: High-
715 resolution ^{17}O and ^{27}Al MAS NMR results. Am. Mineral. 96, 841–853.

716 Toplis, M.J., Dingwell, D.B., Lenci, T., 1997. Peraluminous viscosity maxima in Na_2O-
717 Al_2O_3-SiO_2 liquids: the role of triclusters in tectosilicate melts. Geochim. et Cosmochim. Acta
718 61, 2605–2612.

719 Vuilleumier, R., Seitsonen, A.P., Sator, N., Guillot, N., 2015. Carbon dioxide in silicate melts
720 at upper mantle conditions: Insights from atomistic simulations. Chem. Geol. 418, 77–88.

721 Wallace, M.E., Green, D.H., 1988. An experimental determination of primary carbonatite
722 magma composition. Nature 335, 343–346.

723 Webb, S.L., Knoche, R., 1996. The glass-transition, structural relaxation and shear viscosity
724 of silicate melts. Chem. Geol. 128, 165–183.

White, B.S., Montana, A., 1990. The effect of H_2O and CO_2 on the viscosity of sanidine liquid at high pressures. J. Geophys. Res. B 95, 15683-15693.

Wyllie, P.J., Huang, W.L., 1976. Carbonation and melting reactions in the system CaO–MgO–SiO_2–CO_2 at mantle pressures with geophysical and petrological applications. Contrib. Mineral. Petrol. 54, 79–107.

Xue, X., Kanzaki, M., 2004. Dissolution mechanisms of water in depolymerised silicate melts: constraints from ^{1}H and ^{29}Si NMR spectroscopy and ab initio calculations. Geochim. et Cosmochim. Acta 68, 5027–5057.

Ye, F, Zhu, J., Yu, K., Zhu, R., Xu, Y., Chen, J., Chen, L., 2016. Physicochemical properties of binary mixtures of 1,1,3,3-tetramethylguanidine imidazolide ionic liquid with water and alcohols. J. Chem. Thermo. 97, 39-47.

Zhang, P., Grandinetti, P.J., Stebbins, J.F., 1997. Anionic species determination in $CaSiO_3$ glass using two-dimensional ^{29}Si NMR. J. Phys. Chem. B 101, 4004–4008.

Figure caption:

Figure 1: A, CO_2-bearing glass ^{29}Si NMR spectra simulated with three individual Gaussian lines: Q^1, Q^2 and Q^3 at -76.3, -81.9 and -88.3 ppm, respectively. The CO_2 content calculated as a molar fraction (XCO_2) is reported next to each spectrum. B, CO_2-bearing glass ^{17}O NMR spectra simulated with four individual Gaussian lines: oxygen triclusters (O^{III}) at ~-27 ppm, bridging oxygens ((Si,Al)-BO) at ~+40 ppm, non-bridging oxygens (Ca-NBO) at ~+101 ppm and carbonate groups (CO_3^{2-}) at ~+149 ppm.

Figure 2: Differential Scanning Calorimetric curves measuring the Heat Flow (mW) as a function of the temperature for different glass samples. Thermo-Gravimetric Analysis (TGA) as a function of temperature measuring the weight loss in mg during heating. The glass transition temperature is determined using the three point definition and double tangent method (Morizet et al., 2015a). Weight loss occurs above Tg suggesting that the determined Tg corresponds to the Tg at the measured volatile content.

Figure 3: Deviation in the degree of polymerization (DDP) as a function of CO_2 content. The deviation is calculated as the ratio in between the NBO/T determined from ^{17}O (*filled symbol*) and ^{29}Si (*open symbol*) NMR results and the NBO/T determined from EPMA analyses (see Table 1). Theoretical line corresponds to a constant degree of polymerization; Dissolution line (*red line*) corresponds to the deviation in the degree of polymerization following the dissolution mechanism reported in Eq. 1.

Figure 4: Evolution of the Q^n species as a function of XCO_2. The data points represent the Q^n molar fraction determined by ^{29}Si NMR spectral deconvolution shown in Figure 1. The straight lines represent linear regression for the change in Q^n species. The slope coefficients have then been used to establish the chemical reaction of Eq. 3.

Figure 5: Change in glass transition temperature (Tg) as a function of the DDP measured by ^{29}Si NMR. The XCO_2 is reported for each data point. The assumed error is 10% in relative for the DDP and ±10°C for Tg. This figure highlights the inconsistency between molecular structure and physical properties changes since decreasing DDP is consistent with increasing polymerization whereas decreasing Tg is consistent with decreasing viscosity.

Figure 6: CO_2-bearing silicate melt viscosity as a function of CO_2 content. The model calculation is conducted at 1750K. The XCO_2 is calculated from the EPMA results in Table 1. Three different calculations are performed: constant silicate melt viscosity and increasing carbonate proportion in the liquid mixture ($X_{SL}\eta_{SL\ Init.} + X_{CL}\eta_{CL}$); increasing silicate melt viscosity calculated from the model of Giordano and Russell (2007) due to the progressive depletion in Ca (η_{SL}); combined effect, increasing silicate melt viscosity and decreasing silicate melt fraction with increasing carbonate liquid fraction at constant viscosity obtained from Kono et al. (2014) ($X_{SL}\eta_{SL} + X_{CL}\eta_{CL}$).

Table caption:

Table 1: Experimental pressure; major element concentrations determined by EPMA; volatile content determined from Raman spectroscopy.

Table 2: Degree of polymerization expressed as the NBO/T from EPMA and ^{29}Si and ^{17}O NMR spectroscopy. Glass transition temperature obtained by Differential Scanning Calorimetric measurements.

Table 1:

Sample	Pressure (GPa)	Wt.% SiO_2	Wt.% Al_2O_3	Wt.% CaO	Wt.% Na_2O	Total wt.%	NBO/T[b]	Wt.% H_2O[c]	CO_3/HF Raman[e]	Wt.% CO_2 Raman[d]	XCO_2[e]
RB8 Theoretical[a]		*37.5*	*10.6*	*46.2*	*5.7*		*1.96*				
RB8E-6	0.5	32.1 (0.3)	9.8 (0.2)	42.9 (0.3)	5.9 (0.2)	90.8	2.12	0.6 (0.2)	0.46 ±0.02	6.2 ±0.3	0.086
RB8E-7	0.5	33.3 (0.4)	8.7 (0.2)	41.8 (0.3)	2.7 (0.3	89.5	2.08	0.7 (0.1)	0.48 ±0.01	6.5 ±0.1	0.091
RB8-2	0.5	33.2 (0.3)	9.8 (0.2)	40.4 (0.2)	4.9 (0.1)	88.3	1.92	0.5 (0.1)	0.45 ±0.02	6.0 ±0.3	0.086
RB8E-13	1.0	30.1 (0.4)	8.6 (0.2)	36.0 (0.4)	5.0 (0.2)	79.6	1.92	1.3 (0.1)	0.57 ±0.10	7.7 ±1.4	0.118
RB8E-12	1.0	30.3 (0.6)	8.1 (0.2)	39.8 (0.3)	4.8 (0.1)	83.0	2.14	1.5 (0.1)	0.94 ±0.04	12.6 ±0.5	0.173
RB8E-3	1.5	30.1 (0.2)	8.7 (0.2)	39.4 (0.2)	5.5 (0.3)	83.8	2.11	0.6 (0.1)	1.27 ±0.01	17.2 ±0.1	0.220
RB8-1	1.5	31.3 (0.5)	9.3 (0.2)	37.9 (0.5)	4.4 (0.2)	82.9	1.88	0.6 (0.2)	1.27 ±0.01	17.1 ±0.1	0.221
RB8E-8	1.5	30.1 (0.3)	9.3 (0.2)	36.8 (0.3)	4.9 (0.3)	81.1	1.89	2.8 (0.1)	1.23 ±0.02	16.6 ±0.3	0.221
RB8E-11	1.5	29.7 (0.5)	8.0 (0.1)	38.6 (0.3)	4.6 (0.1)	80.8	2.11	0.9 (0.1)	1.33 ±0.01	18.0 ±0.1	0.234

[a] The RB8 theoretical composition is similar to the one studied in Brooker et al. (2001).

[b] The NBO/T corresponds to the concentration of Non-Bridging Oxygen per Tetrahedron and is calculated from the chemical composition given in the Table 1. The NBO concentration corresponds to the excess negative charges brought by the oxygen in each oxide. This excess negative charge is subsequently divided by the positive charges on tetrahedra which is represented by the molar concentration of Si^{4+} and Al^{3+}.

[c] The H_2O content was determined by FTIR, summing the contribution of the OH^- and H_2O^{mol} vibrational peaks at 4500 and 5200 cm^{-1}, respectively. The error does not exceed ±0.2 wt.% H_2O and corresponds to the standard deviation obtained on the replicated measurements.

[d] The CO_2 solubility has been determined using the method of Morizet et al. (2013) and using the derived CO_3/HF value obtained from the deconvolution of the Raman spectra shown in Figure S3 and subsequent parameters in the Supplementary material 2. The linear relationship has been re-evaluated and is wt.% CO_2 = 13.5 x CO_3/HF. The actual reported error corresponds to the standard deviation of the CO_3/HF ratio obtained from the replicated spectra and shows the global homogeneity of the glass samples. As discussed in the text and mentioned in Table 1, the assumed typical error on the CO_2 solubility using Raman method is 10% in relative to the value.

[e] The XCO_2 has been calculated from the wt.% CO_2 determined by Raman spectroscopy and from the major element concentrations (in wt.%). We used the same error as for the wt.% CO_2 content (10% in relative to the value).

Table 2:

Sample	XCO_2	NBO/T from EPMA[a]	Q^1	Q^2	Q^3	NBO/T from ^{29}Si[b]	(Si,Al)-BO	Ca-NBO	O^{III}	CO_3^{2-}	NBO/T from ^{17}O[c]	DDP ^{29}Si NMR/EPMA	DDP ^{17}O NMR/EPMA	Tg (°C)[f]
RB8E6	0.086	2.12	0.677	0.334	-0.011	1.98						0.93		571
RB82	0.086	1.92	0.414	0.444	0.141	1.69						0.88		526
RB8E7	0.091	2.08					0.379	0.479	0.038	0.104	2.14		1.03	
RB8E13[d]	0.118	1.92	0.388	0.542	0.070	1.73	0.419	0.450	0.054	0.076	1.95	0.90	1.02	
RB8E12	0.173	2.14	0.222	0.493	0.285	1.47	0.429	0.384	0.040	0.146	1.80	0.69	0.84	
RB8E3	0.220	2.11	0.228	0.617	0.156	1.55						0.73		513
RB81	0.221	1.88	0.188	0.425	0.387	1.33						0.71		475
RB8E8[e]	0.221	1.89	0.214	0.393	0.394	1.33						0.70		
RB8E11	0.234	2.11	0.133	0.503	0.364	1.34	0.447	0.344	0.033	0.176	1.67	0.64	0.79	

[a] The NBO/T from EPMA has been calculated from the major element concentrations on a stoichiometric basis.
[b] The NBO/T from ^{29}Si NMR is calculated from the Q^n species concentration. We used the following relation $NBO/Si = 3XQ^1 + 2XQ^2 + XQ^3$; the NBO/T is calculated from the NBO/Si and considering the XAl determined by EPMA. In the calculation Al atoms are considered to be fourfold coordinated.
[c] The NBO/T from ^{17}O NMR is calculated using the following equation: $NBO/T = 4\ X(Ca\text{-}NBO) / (X(Ca\text{-}NBO) + X((Si,Al)\text{-}BO) + X(O^{III})$. The CO_3^{2-} is not included in the calculation considering that CO_2 dissolves as $Ca^{2+}..CO_3^{2-}$.
[d] Sample RB8E13 has been synthesized at 1.0 GPa with undersaturated conditions. The initial CO_2 content loaded was 8.8 wt.%.
[e] Sample RB8E8 has been synthesized in a mixed H_2O-CO_2 fluid phase composition. 6.9 wt.% H_2O was loaded into the capsule prior to the experiment. Micro-FTIR measurements lead to 2.8 wt.% H_2O in the recovered glass.
[f] The glass transition temperature was determined by DSC measurement using the double tangent definition (see Supplementary material 1). Tg is a proxy to melt viscosity and represents a temperature of equal relaxation times.

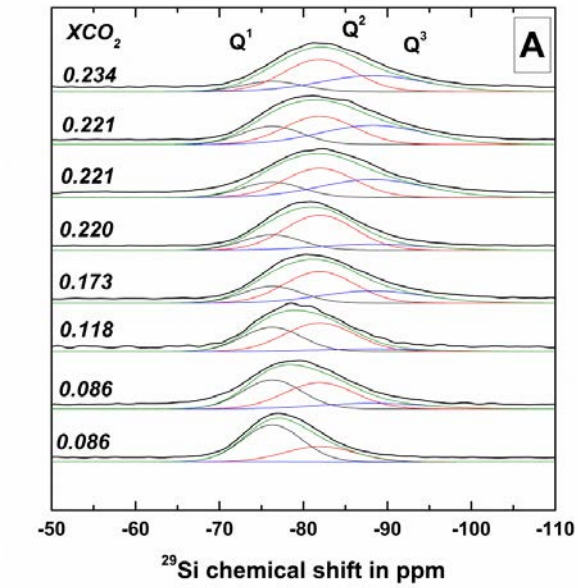
XCO2
Q1
Q2
Q3
A
0.234
0.221
0.221
0.220
0.173
0.118
0.086
0.086
-50 -60 -70 -80 -90 -100 -110
29Si chemical shift in ppm

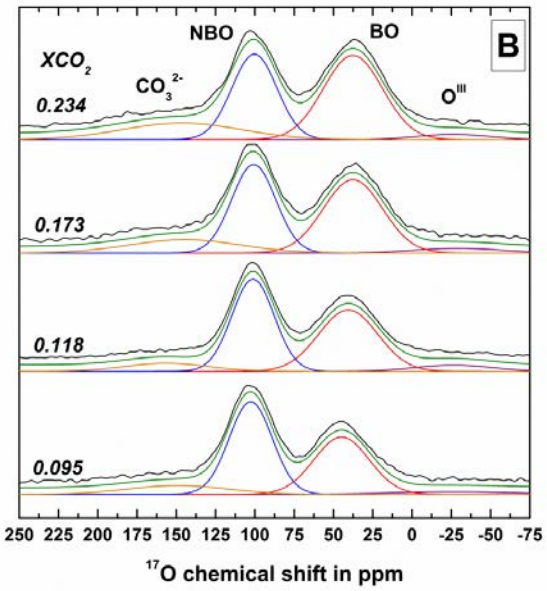
XCO2
NBO
BO
B
CO3 2-
OIII
0.234
0.173
0.118
0.095
250 225 200 175 150 125 100 75 50 25 0 -25 -50 -75
17O chemical shift in ppm

Figure 1

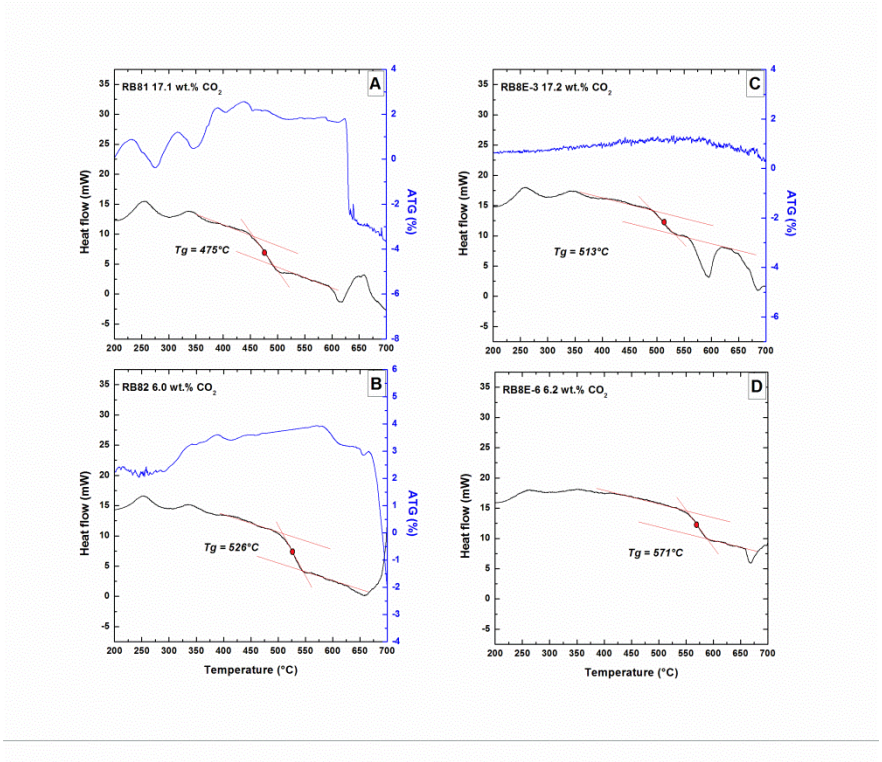
RB81 17.1 wt.% CO2
A
Tg = 475°C
RB8E-3 17.2 wt.% CO2
C
Tg = 513°C
RB82 6.0 wt.% CO2
B
Tg = 526°C
RB8E-6 6.2 wt.% CO2
D
Tg = 571°C
Heat flow (mW)
ATG (%)
Temperature (°C)

Figure 2

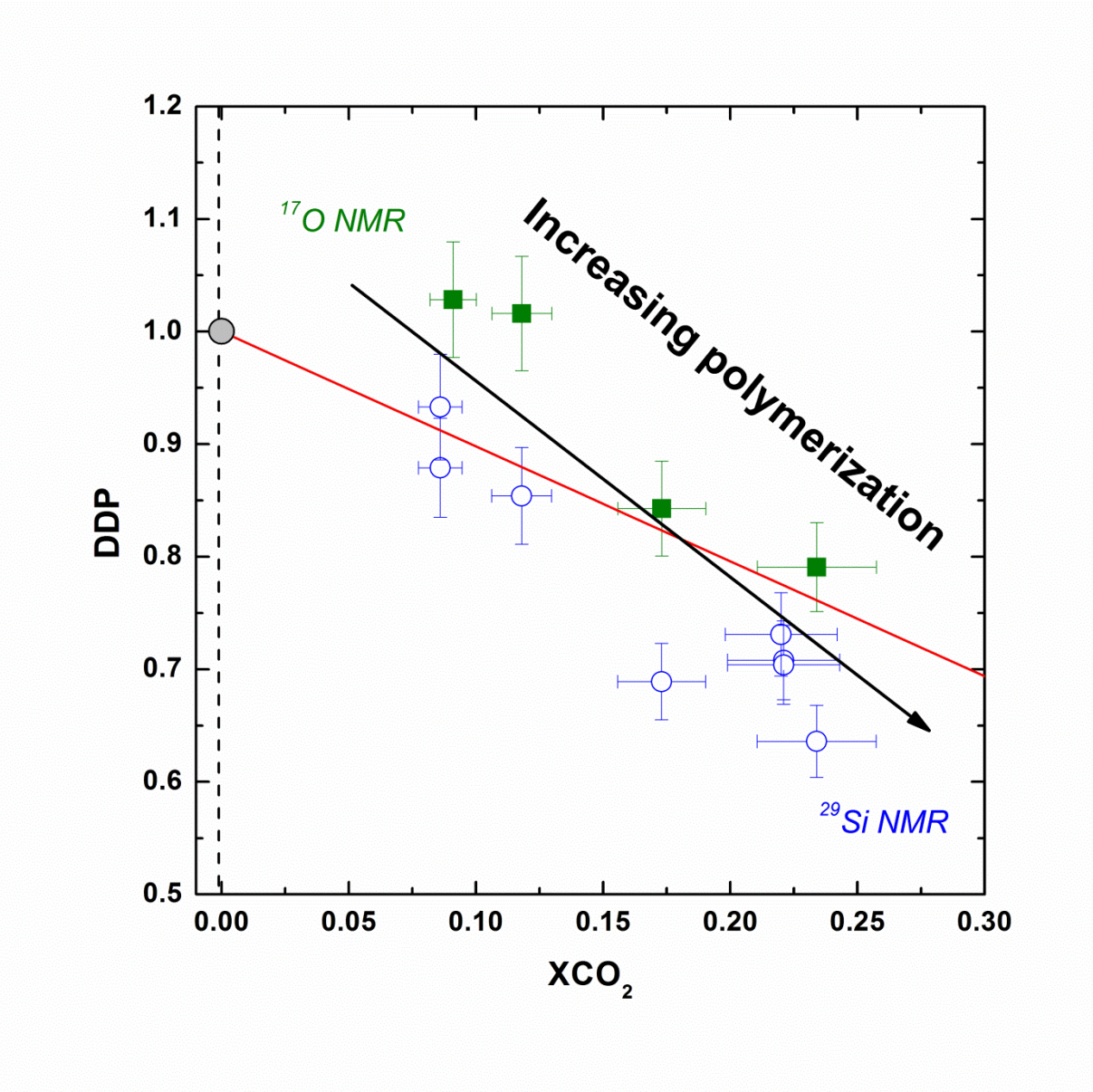
1.2
1.1
1.0
0.9
0.8
0.7
0.6
0.5
DDP
0.00
0.05
0.10
0.15
0.20
0.25
0.30
XCO2
17O NMR
29Si NMR
Increasing polymerization

Figure 3

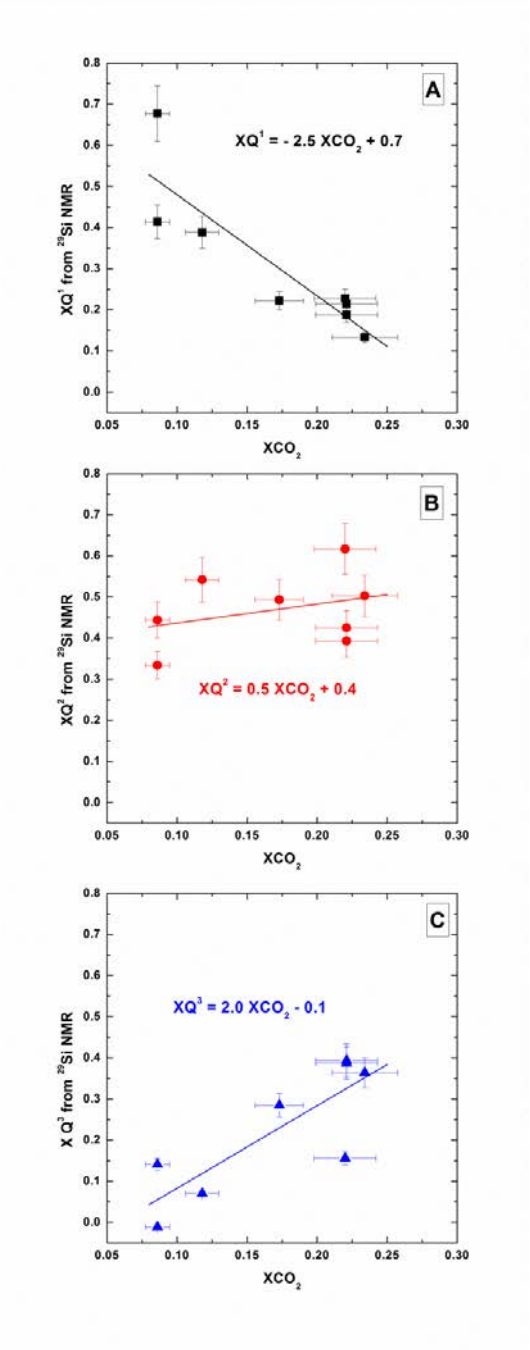
A
$XQ^1 = -2.5\ XCO_2 + 0.7$
XQ^1 from ^{29}Si NMR
XCO_2
B
$XQ^2 = 0.5\ XCO_2 + 0.4$
XQ^2 from ^{29}Si NMR
XCO_2
C
$XQ^3 = 2.0\ XCO_2 - 0.1$
XQ^3 from ^{29}Si NMR
XCO_2

Figure 4

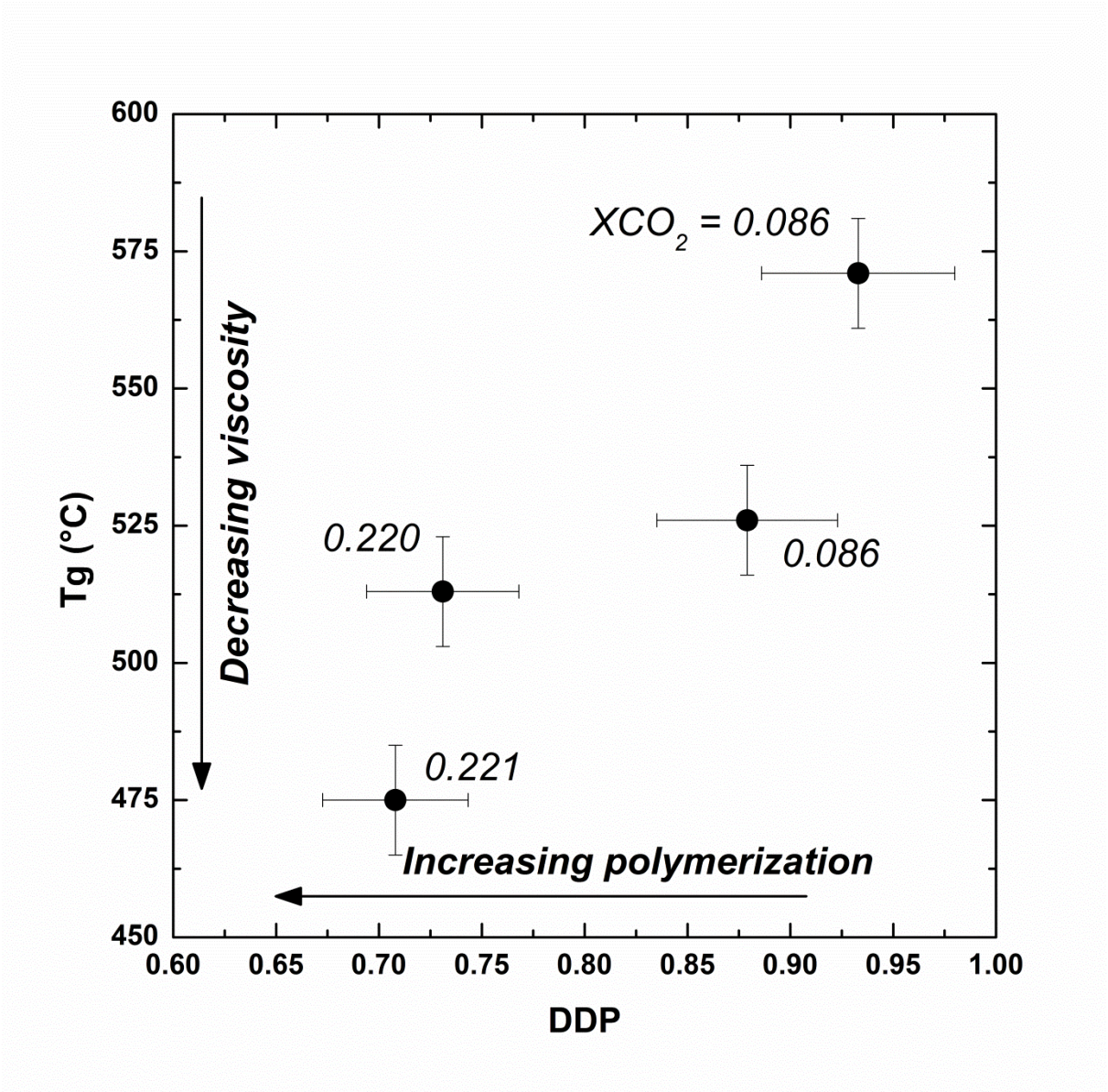
600
575
550
525
500
475
450
Tg (°C)
0.60
0.65
0.70
0.75
0.80
0.85
0.90
0.95
1.00
DDP
Decreasing viscosity
Increasing polymerization
XCO2 = 0.086
0.086
0.220
0.221

Figure 5

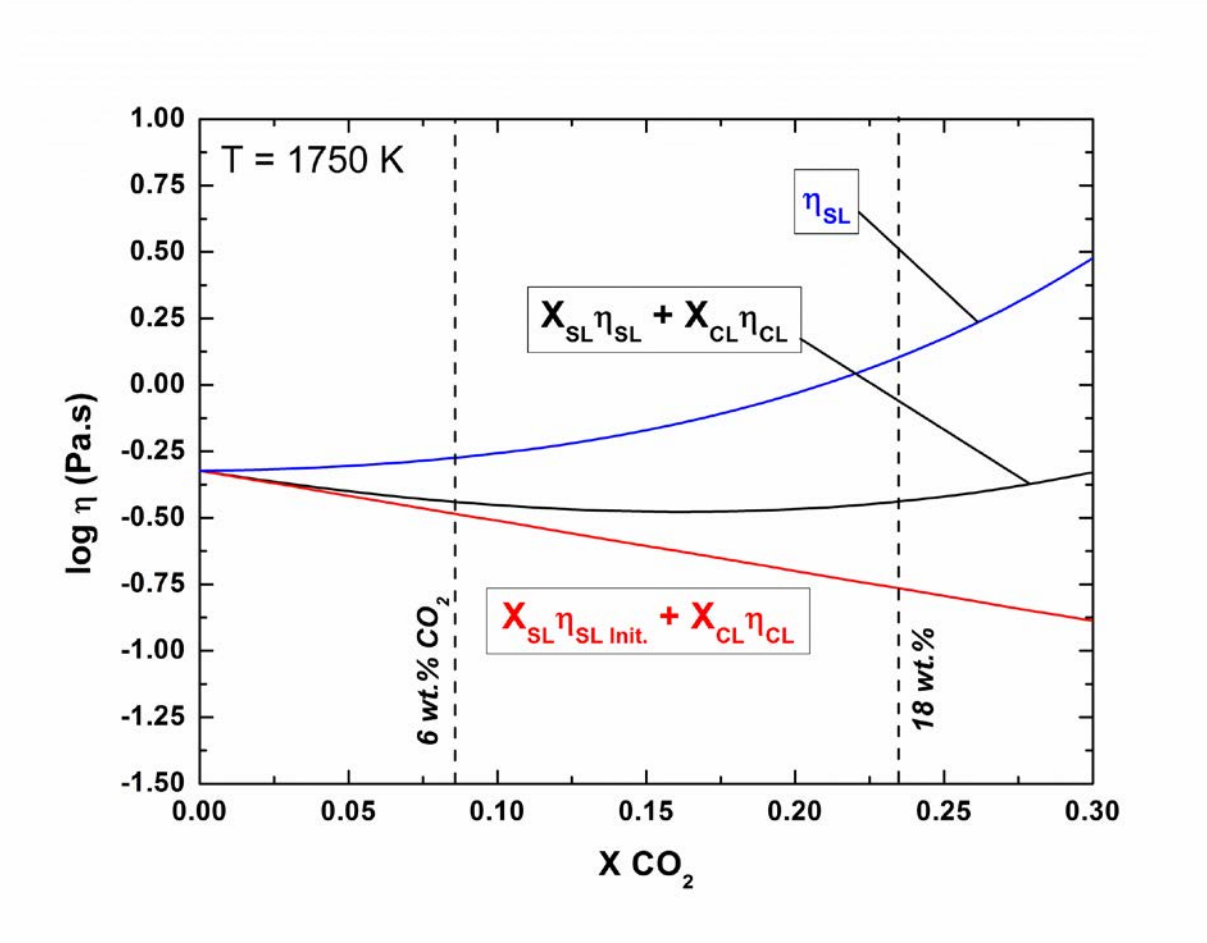
T = 1750 K
η_{SL}
$X_{SL}\eta_{SL} + X_{CL}\eta_{CL}$
$X_{SL}\eta_{SL\ Init.} + X_{CL}\eta_{CL}$
6 wt.% CO_2
18 wt.%
log η (Pa.s)
X CO_2
1.00
0.75
0.50
0.25
0.00
-0.25
-0.50
-0.75
-1.00
-1.25
-1.50
0.00
0.05
0.10
0.15
0.20
0.25
0.30

Figure 6